Semi-Analytical 3D solution for assessing radial collector well pumping impacts on groundwater-surface water interaction

Ali A. Ameli[1] **and James R. Craig**[2]

[1] Global Institute for Water Security, University of Saskatchewan, Saskatoon, Saskatchewan, Canada

[2]University of Waterloo, Department of Civil and Environmental Engineering, Waterloo, Ontario, Canada

Author pre-print

This is the pre-peer reviewed version of the following accepted article:
Ameli, A. A and J. Craig (2017). Semi-Analytical 3D solution for assessing radial collector well pumping impacts on groundwater-surface water interaction, *hydrology research*,
doi: 10.2166/nh.2017.201.

Running title: Pumping impacts on groundwater-surface water interaction

Requests for reprints and correspondence to:

Ali A. Ameli, *PhD, EIT*

Global Institute for Water Security,

University of Saskatchewan, Saskatoon,

Saskatchewan, Canada

Email: ali.ameli@usask.ca

ABSTRACT

We present a new semi-analytical flow and transport model for the simulation of 3-D steady-state flow and particle movement between groundwater, a surface water body and a radial collector well in geometrically complex unconfined aquifers. This precise and grid-free Series Solution-Analytic Element Method (AEM) approach handles the irregular configurations of radial wells more efficiently than grid-based methods. This method is then used to explore how pumping well location and river shape interact and together influence (1) Transit Time Distribution (TTD) of captured water in a radial collector well and TTD of groundwater discharged into the river and (2) the percentage of well waters captured from different sources. Results show that river shape plays a significant role in controlling the aforementioned metrics and that increasing the pumping rate has different consequences in different situations. This approach can also be useful in the design of water remediation and groundwater protection systems (e.g., River Bank Filtration and Well Head Protection Area).

Keywords

Series Solution-Analytic Element Method, Groundwater-surface water interaction, Radial collector well, River Bank Filtration, Transit Time Distribution, Well Head Protection Area

INTRODUCTION

Large quantities of groundwater and induced surface water may be withdrawn by pumping wells. While vertical wells are most common, radial collector wells are sometimes used both for water withdrawal and for remediation of contaminated groundwater systems (e.g., Bakker et al. 2005; Yeh and Chang 2013). The radial collector well is typically composed of a group of horizontal wells which radially extend from a caisson. Modeling of the interaction between groundwater, surface water and radial collector wells can provide useful insights into the physics of this complex interaction.

Grid-based numerical models have been widely used to investigate transient flow and advective particle movement between regional groundwater, surface water and wells using finite element (Ameli and Abedini 2015) and finite difference methods (Haitjema et al. 2010; Rushton and Brassington 2013). However, flow to a radial collector well is usually a multi-scale problem that is challenging if grid-based numerical methods are used. To ensure a proper representation of each radial arm with an arbitrary orientation and a small diameter, these models require a high grid resolution, which may lead to computational inefficiency. For example, to properly obtain the drawdown-discharge relationship of a single horizontal well in a small homogeneous aquifer with a regular geometry (a domain of 150m x 480m x 24m), Haitjema et al. (2010) used a MODFLOW model of 1,846,314 cells. The implementation of the boundary condition along the well screen is also challenging in standard numerical models (Bakker et al. 2005). Flow toward radial arms cannot be explicitly incorporated and is approximated using head dependent boundary cells (Patel et al. 2010) or the drain package (Kelson 2012) accompanied by an entry resistance (conductance factor) in MODFLOW. Additionally, to simulate particle transport, use of a non-uniform Random Walk Particle Tracking (RWPT) scheme or Advection-Dispersion-Reaction (ADR) equation within grid-based flow simulators can be computationally expensive, and can be subject to numerical dispersion and artificial oscillations in the vicinity of each radial arm (Starn *et al.* 2012; Zhan and Sun 2007).

Grid-free analytical methods are also used for the simulation of pumping impacts in geometrically simplified groundwater systems (e.g., Chang and Yeh 2007; Luther and Haitjema 2000). For example, Analytic Element Method (AEM) is an efficient analytical scheme to emulate the 3D impacts of arbitrarily oriented pumping wells. The basic idea behind AEM is the representation of pumping wells by analytic elements (e.g., point sink, line sink), where each element has an analytic solution which satisfies exactly the groundwater governing equation. A line sink with a variable strength distribution may represent each arbitrarily oriented well screen, which can realistically and efficiently emulate the non-uniform flow behavior in the vicinity of a long well screen (e.g., Luther and Haitjema 1999; Steward and Jin 2003); no horizontal or vertical grid discretization is typically required. AEM-based models therefore have been widely developed for the simulation of 2-D and 3-D flow toward vertical well (Bakker 2010; Luther and Haitjema 1999), horizontal well (Bakker and Strack 2003; Haitjema et al. 2010; Steward and Jin 2003) and radial collector wells (Luther and Haitjema 2000; Patel et al. 2010) in aquifers with homogeneous properties. Furthermore, analytical models including AEM can provide fast, precise and continuous particle tracking solutions of flow paths and transit time toward arbitrarily oriented pumping wells (Basu et al. 2012; Haitjema 1995; Zhou and Haitjema 2012). However, in analytical flow and particle tracking models, the surface water geometry and groundwater-surface water interaction are typically simplified. Indeed, these models cannot properly emulate 1) irregular geometry and variable material property (e.g., layer stratification) of the aquifer and surface water bodies and 2) complex 3D flow and particle movement among groundwater, radial collector well and surface water.

Grid-free semi-analytical methods, which benefit from the strength of both analytical and numerical schemes, can alternatively be used to address challenging groundwater-surface water interaction problems with or without pumping wells. For example, Ameli and Craig (2014) and Ameli et al. (2013) have relaxed the constraints of traditional Series Solutions analytical method by enhancing this scheme with a simple numerical least square algorithm. The resulting semi-analytical free boundary groundwater-surface water interaction models have recently been used and tested to simulate 2-D and 3-D saturated-unsaturated flow in geometrically complex multi-layer unconfined aquifers with various patterns of vertical heterogeneity (Ameli *et al.* 2016a; Ameli *et al.* 2016b). These approaches have also been extended to explore the hydrological controls on subsurface transit time distribution (Ameli et al. 2016a), subsurface transport of sorbing contaminants (Ameli 2016) and weathering evolution in the critical zones (Ameli *et al.* 2017). In addition to naturally complex aquifer geometry and stratification, and free boundary conditions applied at water table surface, the geometry and properties of surface water bodies (e.g., lake, river and seepage faces) are appropriately handled in these semi-analytical series solution models.

Here we combine the benefits of AEM and the series solution method to develop a general new groundwater-surface water interaction model in the vicinity of radial collector wells. Based on superposition, the free boundary series solution model developed by Ameli and Craig (2014) for 3-D groundwater-surface water interaction is augmented with a set of analytic elements (line sinks) used to represent a radial collector well. The coupled Series-AEM model is able to provide a "continuous" map of velocity and dispersion tensors in the entire domain which facilitates an efficient simulation of advective-dispersive transport through implementation of a continuous non-uniform RWPT scheme. Our integrated flow and transport scheme 1) exactly satisfies the governing equations of saturated flow, 2) precisely meets boundary conditions and 3) continuously tracks particles all the way from water table to surface water and to a radial collector well without discretization artifacts.

By applying our new integrated flow and transport model presented here to two hypothetical situations we demonstrate that it can be a robust tool for simulating complex interaction between radial collector wells, groundwater, the water table and surface water bodies, including rivers and lakes. The model can determine subsurface flow pathline distribution, source zone extent and the percentage of well water captured from different sources. Potential uses of the model include determining wellhead protection areas and designing contaminant remediation approaches such as river bank filtration or pump and treat systems.

METHOD

FLOW SOLUTION

Figure 1 shows the general layout of a 3-D stratified geometrically complex unconfined aquifer in the presence of a radial collector well and a surface water body. The steady-state problem is posed in terms of a discharge potential, ϕ_m [L^2T^{-1}], defined as

$$\phi_m(x,y,z) = K_m\, h_m(x,y,z) \quad (1)$$

where $h_m(x,y,z)$ [L] and K_m [L/T] are the total hydraulic head and saturated hydraulic conductivity in the m^{th} layer, respectively. Using continuity of mass and Darcy's law, each layer's discharge potential function must satisfy the Laplace equation implying homogeneity and isotropy assumptions in each layer:

$$\frac{\partial^2\phi_m}{\partial x^2} + \frac{\partial^2\phi_m}{\partial y^2} + \frac{\partial^2\phi_m}{\partial z^2} = 0 \quad \text{for } m = 1,\ldots,M \quad (2)$$

Both the series solutions and AEM models can satisfy the linear 3-D Laplace equation (Equation 2) (Ameli and Craig 2014; Steward and Jin 2003). Therefore superposition theorem suggests that in each layer ($m = 1 \ldots M$) of a stratified unconfined aquifer, a discharge potential function of the following form can satisfy equation 2:

$$\phi_m(x,y,z) = \phi_m^{Series}(x,y,z) + \phi^{AEM}(x,y,z) \tag{3}$$

The above equation is the general steady-state Series-AEM solution to groundwater-surface water interaction flow in the vicinity of a radial collector well where ϕ_m^{Series} (Equation A.1) is the 3-D series solution to steady-state groundwater-surface water interaction flow at m^{th} layer of an unconfined aquifer and ϕ^{AEM} (Equation A.2) is the AEM solution representing the presence of radial collector well. The mathematical formulation of both series solution and AEM portions of the equation 3 as well as the implementation of boundary conditions, including free boundary condition along an initially unknown water table location, are explained in the Appendix A.

TRANSPORT SOLUTION

Derivatives of the discharge potential (equation 3) with respect to *x*, *y* and *z* provide a continuous field of Darcy fluxes in the *x* ((q_x (x,y,z)), *y* ((q_y (x,y,z)) and *z* ((q_z (x,y,z)) directions throughout the entire saturated zone. Continuous fields of mean pore water velocity (V_x, V_y and V_z) subsequently are obtained by dividing Darcy fluxes by porosity. These velocities can then be used in non-uniform Random Walk Particle Tracking (RWPT) scheme to track particles and determine their transit times toward surface water bodies and/or radial collector well as explained in Appendix D.

MODEL EFFICIENCY

This section describes an example used to demonstrate the numerical efficiency of the Series -AEM approach for simulation of the interactions between groundwater, a surface water body and a radial collector well in a geometrically complex 2-layer unconfined aquifer. In this example, the radial collector well is composed of 2 arms of the same length of $l_{wl} = 100$ m and diameter of 0.5 m located at an elevation of z_{wl}=7 m, in close vicinity of a surface water body (figure 2). A predefined uniform head of $H_r = 84.15$ m is considered along the surface water body. The hydrological and hydrogeological parameters used are: $K_1 = 100\ \mathrm{m/d}$, $K_2 = 80\ \mathrm{m/d}$, R (recharge infiltration rate) =10^{-2} m/d and Q (pumping rate) =10000 $\mathrm{m^3}$/d.

FLOW SOLUTION

The flow solution and water table location (figure 2) were obtained using an iterative scheme to locate the water table surface (Equation A.8) and the least square method to minimize the errors in each iteration (Appendix B). The solutions were obtained using NC_x= 192 and NC_y= 102 control points per interface (the top of modeled domain and layer interface), and NC_w= 180 control points along each radial arm (see Appendix B). A small number of series terms of J = N =30 (Equation A.1), and line segments of N_s=15 (Equation A.2) along each arm is used. To satisfy the no-flow condition along the four sides of the domain for the AEM portion of the solution an additional 17 image wells (as shown in figure A.1) are considered. An additional 18 image wells are also situated below the flat bedrock to satisfy no-flow condition along bottom bedrock for the AEM portion of the solution (Equation A.4). A relaxation factor of τ = 0.10 is also considered in the iteration scheme (Equation A.8).

LEAST SQUARE ERROR

As stated in the Appendix A, the series-AEM solution developed here satisfies the governing equation exactly. The no-flow condition along the bottom bedrock by the AEM portion of the solution was exactly satisfied using 18 additional image wells. The solution and the constraint on total inflow into the radial collector well (equation (A.6)) were met exactly. However, using least squares there are numerical errors in the implementation of boundary and continuity conditions along the top surface, bottom surface (only series solution portion), layer interface and radial arms. The definition of least squares equations used to construct the system of equations, and the equations used to calculate the normalized numerical errors along each interface (i.e. $\varepsilon_1^{\text{flux}}$, $\varepsilon_1^{\text{head}}$, $\varepsilon_2^{\text{flux}}$, $\varepsilon_2^{\text{head}}$, $\varepsilon_{M+1}^{\text{flux}}$, $\varepsilon^{\text{well}}$) are described in Appendix B and Appendix C, respectively. Figure 3a shows the largest normalized flux error ($\varepsilon_1^{\text{flux}}$) across the water table surface occurs directly at the intersection of surface water and aquifer with a maximum of 3%. This error can be attributed to Gibbs phenomenon (Gibbs 1899) at the abrupt transition from Neumann to Dirichlet boundary conditions, where the exact solution is discontinuous. The mean absolute normalized flux error along this interface is 0.04%. At the remaining error evaluation points along the top interface which are in direct contact with the surface water body, the maximum normalized head error ($\varepsilon_1^{\text{head}}$) is on the order of 0.01% (not shown here). The normalized least square errors across the layer interface and bottom bedrock are explained in the caption of figure 3. The head uniformity condition along two radial arms is met with a maximum normalized head error of $\varepsilon^{\text{well}} = 0.01\%$ (not shown here).

GLOBAL MINIMUM OF THE LEAST SQUARE SCHEME

In the original example, an initial water table elevation equal to H_r (water level stage at surface water body) was used within the iterative scheme; 60 iterations were required for the convergence of pressure head along water table to zero (Appendix A). In a separate analysis, to ensure that the solution is robust, seven different initial water table elevations (from z = 10 to z = 70 m) were used; the water table surface for all seven cases converged to the original surface shown in Figure 2b, implying that the least square scheme calculated the global minimum of the system.

FLOW PATHLINE

120 uniformly-spaced particle capture points located at 6 positions along the perimeter of each arm of the well are used to generate pathlines toward radial collector well using back tracking of each captured particle (only 40 pathlines are shown in figure 2a). These pathlines can also be used to approximate the percentage of well waters originating from the surface water body source (S_r), by assigning a flow quantity to each pathline. This flow is equal to one sixth of the calculated strength of the line sink segment (${\sigma_0}^i$) corresponding to the pathline termination location. From the subsurface pathlines in Figure 2a, S_r is estimated as 45%.

RADIAL COLLECTOR WELL IN THE VICINITY OF ARIVER

In the second example, we simulate flow, advective-dispersive particle movement and particle transit time between groundwater, a meandering river and a radial collector well in a homogenous unconfined aquifer with an average vertical thickness of 50 m. This example assesses the impacts of pumping rate and radial collector well location on the percentages of well water captured from different sources, source zone extent and the transit time distribution (TTD) of groundwater discharged into the radial collector well and the river. The land surface topography used for this example (Figure 4) is taken from the Grand River watershed in southern Ontario. The aquifer is assumed to be homogeneous with $K = 100$ m/d, α_L=0.1cm (longitudinal dispersivity of the porous medium; Appendix D), α_T=0.001 cm (transverse dispersivity of the porous medium; Appendix D) and $R = 0.01$ m/d. Along the river, a uniform surface water hydraulic gradient of 0.21 m/km is assumed with a minimum surface water elevation of 50.18 m at downriver (*x* =1200 m) and maximum head of 50.42 m at upriver (*x*=0) of the river.

All the solution parameters (e.g., J, N, N_s) and the layout of image wells are the same as in the first example. The solution for this hypothetical example was obtained successfully, with least square errors along evaluation surfaces similar to those in the first example.

SOURCE ZONE EXTENT

Figures 4a and 4a′ show that with the same pumping rate of Q=5,000 m^3/d, the source zone extent of the radial collector wells for the two configurations is significantly different; for configuration B (inside a bend of the river), the source zone extent is highly controlled by the river shape. The depleted flux distribution also demonstrates that, for configuration B, higher fluxes of river water with a maximum of 0.09 m/d is depleted from a small part of the river while this maximum value for configuration A (beside a straight portion of the river) is 0.02 m/d. As can be expected the percentage of captured well water originated from river (S_r) for position B (70%) is considerably larger than configuration A (11%). For larger pumping rates, a similar behaviour between two configurations was observed. For Q=10,000 m^3/d (Figures 4b and 4b′) the maximum depleted flux (induced by pumping) at the river bed is 0.18 m/d and 0.07 m/d, with S_r equal to 80% and 39% for pumping at configurations B and A, respectively. For Q=15,000 m^3/d (Figures 4c and 4c′) the water is depleted at the river bed with a maximum of 0.27 m/d and 0.125 m/d, and S_r is equal to 80% and 45% for configurations B and A, respectively. Figure 4 also suggests that by increasing the pumping rate the lateral source zone extent does not change for configuration B while for configuration A this area increases considerably. This can also be seen from the variation of (S_r) by increasing the pumping rate; while S_r for configuration A increases considerably (from 11% to 45%) when pumping rate is tripled (from Q=5,000 m^3/d to Q=15,000 m^3/d), S_r for configuration B increases only from 70% to 80%. As pumping rate increases from Q=10,000 m^3/d to Q=15,000 m^3/d, S_r for configuration B remains constant.

TRANSIT TIME DISTRIBUTION

Transit time (or groundwater age) of water particles (the elapsed time that particles spend traveling through subsurface; Appendix D) and transit time distribution (the probability density function of transit times; Appendix D) of water particles discharged into the river and/or radial collector are also influenced by pumping rate and the location of radial collector well.

Figure 5a&a′ shows that for position A of the collector well, as pumping rate increases from 5000 to 15000 m^3/d, the mean groundwater age and the proportion of early and late arrival waters discharged into the river considerably decreases. The Gamma shape parameter of the probability density function of transit times increases from 0.78 to 1.03 which implies a decrease in the age variability of water discharged into the river. For position B, however, as pumping rate increases the Gamma shape parameter only slightly increases from 0.78 to 0.84 with a smaller decrease in the percentages of early and late arrival of the water particles discharged into the river, and a smaller decrease in mean groundwater age of the water particles discharged into the river compered to position A.

Figure 5b&b′ shows for position A of the radial collector well, the percentage of both early and late arrival waters (relative to mean groundwater age) captured by radial collector well increases smoothly as pumping rate increases from 5000 m^3/d to 15000 m^3/d. The ensemble of mean groundwater age from both groundwater and river sources discharged to the radial collector well decreases from 1585 to 847 days. For position B, again, the percentages of both early and late arrival waters (relative to mean groundwater age) captured by the radial collector well increases as pumping rates increases; however, here there is a sharper decay in early transit times compared to position A. This can be intimately tied to the small source zone extent of the radial collector well located in position B where a high percentages of water particles in the vicinity of the radial collector well (relatively) rapidly captured by the well. The ensemble mean age of water particles captured by the pumping well is significantly younger for the radial collector well located at position B compared to position A.

DISCUSSION:

Results suggest that the semi-analytical series-AEM model developed here is able to precisely address 3-D steady flow and advective-dispersive transport between the radial collector well, regional groundwater and surface water body despite the complicating presence of a free boundary, infiltration and natural geometry and stratification. The groundwater governing equation was satisfied exactly, and boundary conditions were implemented within an acceptable range of error. This precise flow and transport scheme was then used to assess the impact of pumping well rate and placement on (1) groundwater transit time distributions discharged into the surface water body and captured by the well, (2) local source zone extent and (3) the percentage of well waters captured from different sources (groundwater or surface water). Results suggest that the impact of pumping well rate on the aforementioned measures depends mainly on the river shape in the vicinity of pumping well.

The general flow and transport model developed in this paper has the ability to precisely discern the sources of the collector well waters and the percentage of captured well waters from a river (S_r) and/or groundwater. In addition, the grid-free semi-analytical approach presented here can be easily used for various layouts, orientations (e.g., vertical), elevations and length of radial arms; thus it is potentially a useful tool for the engineering design of water remediation and groundwater protection systems.

Results show that increasing the pumping rate does not lead to the same consequences for radial collector wells located at different positions with respect to the river. When the well is surrounded by a meandering branch of the river (position B-Figure 4), increasing the pumping rate can only slightly increase the percentage sourced from river and the source zone extent, but significantly decreases the mean transit time of river water captured by the radial collector well (Figure 5b′). These findings are important for the design of River Bank Filtration (RBF) systems (radial collector wells installed in the vicinity of surface water bodies to withdraw naturally filtered surface water), where the effectiveness of a given radial collector well in a RBF system is assessed by the ability of the well to capture more river water than groundwater but with sufficient transit time so as to filter out undesirable constituents (Moore *et al.* 2012). Our results also show that when in the well is surrounded by a meandering branch of the river a high percentage of early arrival (relative to mean age) water particles captured by the well and this behaviour is enhanced as pumping rate increases (Figure 5b′). This together with significantly shorter mean groundwater ages (for all pumping rates) and smaller source zone extent of the well located at position B suggest that a high percentage of water particles "rapidly" captured from the vicinity of the radial collector well. For example, for the hypothetical well-river interaction example solved here, 95% of water particles are captured in almost two years by the radial collector well at position B when the pumping rate (Q) is 5000 m^3/d but only 3% are captured by the well in position A. This suggests that more stringent protective policies are required in the vicinity of the pumping wells located in the inner section of the bend of meandering rivers (e.g., position B), as a high percentage of water and potential contaminant at the surface (both in surface water body and/or along land surface) is rapidly captured by the well leads to a short time to detect the potential groundwater concern. This finding can inform the protection practices (e.g., Well Head Protection Area systems) required around pumping wells, which are used to supply municipal drinking water.

CONCLUSIONS

A general semi-analytical Series-AEM model for the simulation of 3-D flow and advective-dispersive transport between a radial collector well, groundwater and geometrically complex surface water bodies was developed and assessed. For two hypothetical examples studied here, this grid-free model precisely simulated 3-D groundwater-surface water interaction in the vicinity of radial collector wells; mass balance was satisfied exactly over the entire domain except along layer interfaces and boundaries where boundary and continuity conditions were met with an acceptable range of error. This precise semi-analytical groundwater-surfacewater interaction model showed that the impacts of pumping well rate on (1) the transit time distributions of water particles discharged into a river and an adjacent radial collector well, (2) the local well source zone extent and (3) the percentage of well waters captured from different sources, significantly depend on the river shape in the vicinity of the pumping well. The results demonstrate the value of the model in its practical application to problems of water remediation (e.g., River Bank Filtration system design) and groundwater protection (e.g., Well Head Protection Area determination).

Acknowledgement

We thank four anonymous reviewers of the Hydrology Research journal for their constructive comments.

References

Ameli, A.A. 2016 Controls on subsurface transport of sorbing contaminant. *Hydrology Research*. DOI:10.2166/nh.2016.170

Ameli, A.A. & Abedini, M.J. 2015 Performance assessment of low-order versus high-order numerical schemes in the numerical simulation of aquifer flow. *Hydrology Research*. DOI:10.2166/nh.2016.148

Ameli, A.A. et al. 2016a Hillslope permeability architecture controls on subsurface transit time distribution and flow paths. *Journal of Hydrology*, **543**: 17-30. DOI:10.1016/j.jhydrol.2016.04.071

Ameli, A.A. et al. 2017 Primary weathering rates, water transit times and concentration-discharge relations: A theoretical analysis for the critical zone. *Water Resources Research*, **52**. DOI:10.1002/2016WR019448

Ameli, A.A. & Craig, J.R. 2014 Semianalytical series solutions for three-dimensional groundwater-surface water interaction. *Water Resources Research*, **50**(5).

Ameli, A.A., Craig, J.R. & Wong, S. 2013 Series solutions for saturated–unsaturated flow in multi-layer unconfined aquifers. *Advances in Water Resources*, **60**: 24-33.

Ameli, A.A., McDonnell , J.J. & Bishop, K. 2016b The exponential decline in saturated hydraulic conductivity with depth and its effect on water flow paths and transit time distribution. *Hydrological Processes*, **30**(14): 12. DOI:10.1002/hyp.10777

Bakker, M. 2010 Hydraulic modeling of riverbank filtration systems with curved boundaries using analytic elements and series solutions. *Advances in Water Resources*, **33**(8): 813-819.

Bakker, M., Kelson, V.A. & Luther, K.H. 2005 Multilayer Analytic Element Modeling of Radial Collector Wells. *Ground Water*, **0**(0): 050901015612001. DOI:10.1111/j.1745-6584.2005.00116.x

Bakker, M. & Strack, O.D. 2003 Analytic elements for multiaquifer flow. *Journal of Hydrology*, **271**(1): 119-129.

Basu, N.B., Jindal, P., Schilling, K.E., Wolter, C.F. & Takle, E.S. 2012 Evaluation of analytical and numerical approaches for the estimation of groundwater travel time distribution. *Journal of Hydrology*, **475**: 65-73.

Chang, Y.-C. & Yeh, H.-D. 2007 Analytical solution for groundwater flow in an anisotropic sloping aquifer with arbitrarily located multiwells. *Journal of hydrology*, **347**(1): 143-152.

Delay, F. & Bodin, J. 2001 Time domain random walk method to simulate transport by advection-dispersion and matrix diffusion in fracture networks. *Geophysical research letters*, **28**(21): 4051-4054.

Gibbs, J.W. 1899 Fourier's series. *Nature*, **59**(1539): 606.

Haitjema, H. 1995 On the residence time distribution in idealized groundwatersheds. *Journal of Hydrology*, **172**(1): 127-146.

Haitjema, H., Kuzin, S., Kelson, V. & Abrams, D. 2010 Modeling Flow into Horizontal Wells in a Dupuit-Forchheimer Model. *Ground Water*, **48**(6): 878-883. DOI:10.1111/j.1745-6584.2010.00694.x

Kelson, V. 2012 Predicting Collector Well Yields with MODFLOW. *Ground Water*, **50**(6): 918-926. DOI:10.1111/j.1745-6584.2012.00910.x

Luther, K. & Haitjema, H. 2000 Approximate analytic solutions to 3D unconfined groundwater flow within regional 2D models. *Journal of Hydrology*, **229**(3): 101-117.

Luther, K. & Haitjema, H.M. 1999 An analytic element solution to unconfined flow near partially penetrating wells. *Journal of Hydrology*, **226**(3): 197-203.

Moore, R., Kelson, V., Wittman, J. & Rash, V. 2012 A Modeling Framework for the Design of Collector Wells. *Ground Water*, **50**(3): 355-366. DOI:10.1111/j.1745-6584.2011.00850.x

Patel, H., Eldho, T. & Rastogi, A. 2010 Simulation of radial collector well in shallow alluvial riverbed aquifer using analytic element method. *Journal of irrigation and drainage engineering*, **136**(2): 107-119.
Rushton, K.R. & Brassington, F.C. 2013 Significance of hydraulic head gradients within horizontal wells in unconfined aquifers of limited saturated thickness. *Journal of Hydrology*, **492**: 281-289. DOI:10.1016/j.jhydrol.2013.04.006
Salamon, P., Fernàndez-Garcia, D. & Gómez-Hernández, J. 2006 Modeling mass transfer processes using random walk particle tracking. *Water resources research*, **42**(11).
Starn, J.J., Bagtzoglou, A.C. & Robbins, G.A. 2012 Methods for simulating solute breakthrough curves in pumping groundwater wells. *Computers & Geosciences*, **48**: 244-255.
Steward, D.R. & Jin, W. 2003 Drawdown and capture zone topology for nonvertical wells. *Water Resources Research*, **39**(8): n/a-n/a. DOI:10.1029/2002wr001709
Yeh, H.-D. & Chang, Y.-C. 2013 Recent advances in modeling of well hydraulics. *Advances in Water Resources*, **51**: 27-51. DOI:10.1016/j.advwatres.2012.03.006
Zhan, H. & Sun, D. 2007 Travel-time distribution from a finite line contamination source to an extraction well with regional flow. *Advances in water resources*, **30**(3): 389-398.
Zhou, Y. & Haitjema, H. 2012 Approximate solutions for radial travel time and capture zone in unconfined aquifers. *Groundwater*, **50**(5): 799-803.

Appendix A: Mathematical Formulation of Series - AEM solution

The 3-D series solution to steady-state groundwater flow governing equation (Equation 2) at the m^{th} layer is obtained using the method of separation of variables (as was developed in Ameli and Craig 2014) as:

$$\phi_m^{Series}(x,y,z) = \sum_{j=0}^{J-1}\sum_{n=0}^{N-1} \cos\ \omega_j x \cos\omega_n y\ [A_{jn}^m \cosh(\gamma_{jn} z) + B_{jn}^m \sinh(\gamma_{jn} z)] \qquad \text{(A.1)}$$

$$\omega_j = \frac{j\pi}{L_x};\ \omega_n = \frac{n\pi}{L_y};\ \gamma_{jn} = \pi\sqrt{\frac{j^2}{{L_x}^2}+\frac{n^2}{{L_y}^2}}\quad for\ j\ =\ 0\ldots.J-1\ \ \&\,n\ = 0\ldots.N-1$$

In the above equation, ω and γ were obtained by applying no flow boundary conditions at four sides of the domain (Figure 1), j and n represent the coefficient index while J and N are the order of approximation in the x and y direction, respectively (in total, N x J series terms are used). A_{jn}^m, B_{jn}^m are the unknown series coefficients associated with the m^{th} layer.

The AEM solution representing the radial collector well is calculated by superimposing the analytic solutions corresponding to all segments representing the collector well as:

$$\phi^{AEM}(x,y,z) = \sum_{i=1}^{N_s} \phi_w^i(x,y,z) \tag{A.2}$$

$\phi_w^i(x,y,z)$ is the discharge potential corresponding to i^{th} well segment in the global coordinate system and N_s is the number of line segment used to emulate the presence of radial collector well. Note that subscript *w* denotes well properties in the reminder of this paper. By integrating the potential for a set of point sinks along a line segment of a length of $2l$, Steward and Jin (2003) developed a closed form expression representing the discharge potential in local coordinate of the segment. Here, in the global coordinate system of the model, the discharge potential correspond to i^{th} line segment located in *x* direction is defined as follows;

$$\phi_w^i(x,y,z) = -\frac{{\sigma_0}^i}{4\pi} \ln \frac{\left[\left(x - x_0^i + l^i\right)^2 + \left(y - y_0^i\right)^2 + \left(z - z_0^i\right)^2\right]^{\frac{1}{2}} + \left(x - x_0^i + l^i\right)}{\left[\left(x - x_0^i - l^i\right)^2 + \left(y - y_0^i\right)^2 + \left(z - z_0^i\right)^2\right]^{\frac{1}{2}} + \left(x - x_0^i - l^i\right)} \tag{A.3}$$

Where ${\sigma_0}^i$ refers to the a priori *unknown* constant strength of i^{th} segment, and and l^i is the half of the segment length. x_0^i, y_0^i and z_0^i refer to the center of i^{th} segment in the global coordinate system. The method of images (Figure A.1) is here employed to enable AEM part of the solution to satisfy no-flow conditions at the sides of the domain. Therefore equation A.2 is modified as

$$\phi^{AEM}(x,y,z) = \sum_{i=1}^{N_s} \phi_w^i(x,y,z) + \sum_{j=1}^{N_I} \sum_{i=1}^{N_s} \phi_w^{ij}(x,y,z) \tag{A.4}$$

Where ϕ_w^{ij} refers to discharge potential correspond to the image of i^{th} segment and N_I is the number of image wells. Figure A.1 depicts the layout (plan view) of real and image wells, and the images of images wells used in this paper to fulfill the AEM portion of the no-flow condition at the sides of the domain. Note that the no-flow boundary conditions at the sides of the domain are only met exactly when the number of image wells at the four sides approaches infinity. In addition, to mimic no-flow condition at the bottom boundary by AEM portion of the solution, all real and image wells shown in figure A.1 should be placed symmetrically below the bottom bedrock interface as image wells. Using the method of images, the strength associated with each image segment is identical to its real counterpart and only their locations are different. The no-flow condition along the bottom boundary for the series portion of the solution is enforced at control points using a least square numerical scheme (Appendix B).

There are also other boundary conditions which should be applied along the radial collector wells and the boundaries of the computational domain to calculate the unknown coefficients of equations A.1 and A.3. Steward and Jin (2003) have suggested that two boundary conditions must be satisfied along the entire well screen's length. First, the a priori unknown head along the cylindrical face of the well (H_w) must be uniform, which implies zero head loss along the well screens. This is applied by setting the head at a set of NC_w control points (located along screens surface) equal to the head at a specified but arbitrary position p along this boundary.

$$\frac{\phi\left(x_p, y_p, z_p\right)}{K_p} = \frac{\phi_{\dddot{m}}(x_w, y_w, z_w)}{K_{\dddot{m}}} \; for\ w = 1 \dots NC_w \tag{A.5}$$

In equation (A.5), $\dot{m}$ is conditional upon the layer where each control point is located. The uniformity of head condition is met exactly when the number of line sink segments approaches infinity. For the second boundary condition at the collector well, the summation of unknown strengths of consecutive line sink segments along all arms is set equal to the pumping rate Q

$$\sum_{i=1}^{N_s} 2l^i {\sigma_0}^i = Q \tag{A.6}$$

The top of the modeled domain (Figure 1) is the surface defined as the water table surface ($z_{wt}(x,y)$) where the water table is lower than the land surface (recharge areas), and the land surface ($z_1(x,y)$) at areas in direct contact with surface water body. The former is located using an iterative scheme, while the latter (land surface) is known a priori. The top of the modelled domain surface is subject to a specified infiltration rate (R) at recharge areas, and/or Dirichlet boundary conditions along surface water bodies (Figure 1). Continuity of flux and pressure head is required along each layer interface ($m = 2, \ldots, M$). The readers are referred to Ameli and Craig (2014) for a detail discussion of the boundary and continuity conditions and iterative scheme used to locate the water table surface.

The 3-D semi-analytical Series-AEM solution for the interaction between groundwater, surface water bodies and a radial collector well (equation (3)) in each layer of a stratified unconfined aquifer is completed by identifying unknown coefficients of the series solution (A_{jn}^m, B_{jn}^m in equation (A.1)) and AEM terms (${\sigma_0}^i$ in equation (A.3)). These coefficients are calculated using a constrained least squares numerical algorithm to satisfy boundary and continuity conditions at a set of control points. A set of NC control points are located along the water table surface ($z_{wt}^r(x,y)$ where r is the iteration number), bottom boundary ($z_{M+1}(x,y)$)

and each layer interface ($z_m(x, y)$) to implement the aforementioned boundary and continuity conditions using least squares algorithm. Note that here NC is the product of NC_x and NC_y which are the number of uniformly spaced control points in x and y directions, respectively. The uniformity of head boundary condition along the radial screens is satisfied by applying equation A.5 at a set of NC_w control points located along the screens surface. Initially, the water table surface, $z_{wt}^1(x, y)$, is assumed to be equal to the river or other surface water body stage, H_r, at all control points. At each iteration, the unknown coefficients for each guess of the water table surface are calculated by minimizing the total sum of squared boundary and continuity condition errors (at control points along the mentioned interfaces and well screen surfaces) that is constrained with equation A.6 such that the total inflow be equal to pumping rate Q at the radial collector well. The total sum of squared errors (TSSE) at each iteration is subdivided into the errors along mentioned evaluation curves:

$$\mathrm{TSSE} = \mathrm{SSE_t} + \sum_{\mathrm{m}=2}^{M} \mathrm{SSE_m} + \mathrm{SSE_b} + \mathrm{SSE_w} \tag{A.7}$$

The subscript (t) refers to the sum of squares boundary condition errors along the modeled domain surface, subscript (m) refers to the sum of squares continuity errors along the layer interfaces, subscript (b) refers to the sum of squares boundary condition errors along the bedrock interface (series solution portion) and subscript (w) refers to the sum of squares error for the implementation of uniformity of head along radial collector well screens (equation A.5). The equations for sum of squares error along these evaluation curves are included in Appendix B. The unknown series solution and AEM coefficients for each iteration (r), are calculated by minimizing equation A.7. Then, the 3-D Series-AEM expansion for discharge potential (equation 3) is fully obtained; however the zero pressure head condition along the water table surface is still not obtained exactly due to the initially incorrect location of water table. Equation 3 provides a hydraulic head distribution ($h_m^r\big(x_i, y_i, z_{wt}^r(x_i, y_i)\big)$) in each iteration and for each control point along the location of water table surface. Due to the zero pressure head condition along the water table, in each iteration and for each control point, the following equation may be used to update the water table location:

$$z_{wt}^{r+1} = z_{wt}^r + \tau(h_m^r(x_i, y_k, z_{wt}^r) - z_{wt}^r) \tag{A.8}$$

where τ is an under-relaxation factor which is always between 0 and 1. The location of water table is updated in this iterative scheme until the Series-AEM solution converges and $h_m^r(x_i, y_k, z_{wt}^r) - z_{wt}^r$, which represents the error in zero pressure head condition along the water table, approaches zero.

Appendix B: Sum of Squares error equations

The component of the total sum of squares error (equation (A.7)) i.e. sum of squares errors along the evaluation surfaces are as follows:

$$\mathrm{SSE_t} = \sum_{\substack{i=1 \\ i \notin C}}^{NC} \left[\frac{\partial \phi_{\dot{m}}}{\partial \eta}\big(x_i, y_i, z_{wt}^r(x_i, y_i)\big) - R\right]^2 + \sum_{\substack{i=1 \\ i \in C}}^{NC} \left[\frac{\phi_{\dot{m}}\big(x_i, y_i, z_1\ (x_i, y_i)\big)}{K_{\dot{m}}} - H_r\right]^2 \tag{B.1}$$

Where $\mathrm{SSE_t}$ refers to the sum of squares error at NC control points in imposing the recharge infiltration flux (R) along the a priori unknown location of the phreatic surface (Z_{wt}) and constant head (H_r) at areas in direct contact with surface water body. In addition, C is the set of coordinate indices for control points in direct contact with the surface water body and η is the coordinate normal to the phreatic surface.

$$\mathrm{SSE_m} = \sum_{i=1}^{NC}\left[\frac{\partial\phi_m}{\partial\eta}\big(x_i,y_i,z_m(x_i,y_i)\big) - \frac{\partial\phi_{m-1}}{\partial\eta}\big(x_i,y_i,z_m(x_i,y_i)\big)\right]^2 + \sum_{i=1}^{NC}\left[\frac{\phi_m(x_i,y_i,z_m(x_i,y_i))}{K_m} - \frac{\phi_{m-1}(x_i,y_i,z_m(x_i,y_i))}{K_{m-1}}\right]^2 \quad \text{for } m=2, \ldots, M \qquad \text{(B.2)}$$

$$\mathrm{SSE_b} = \sum_{i=1}^{NC}\left[\frac{\partial\phi_M}{\partial\eta}\big(x_i,y_i,z_{M+1}(x_i,y_i)\big)\right]^2 \qquad \text{(B.3)}$$

$\mathrm{SSE_m}$ refers to the sum of squares error at NC control points in applying continuity of flux and head across the layer interfaces, and $\mathrm{SSE_b}$ refers to the sum of squares error at NC control points located along the bottom boundary used to impose no-flow condition (series solution portion). Again, η is the coordinate normal to the layer interfaces or bottom boundary.

$$\mathbf{SSE_w} = \sum_{\mathbf{w=1}}^{\mathbf{NC_w}}\left[\frac{\boldsymbol{\phi}_{\ddot{\mathbf{m}}}(\mathbf{x_w},\mathbf{y_w},\mathbf{z_w})}{\mathbf{K}_{\ddot{\mathbf{m}}}} - \frac{\boldsymbol{\phi}\,(\mathbf{x_p},\mathbf{y_p},\mathbf{z_p})}{\mathbf{K_p}}\right]^{\mathbf{2}} \qquad \text{(B.4)}$$

$\mathrm{SSE_w}$ refers to the sum of squares error at NC_w control points located along the radial collector well screens to impose uniformity of head condition (equations A.5).

Appendix C: Boundary and Continuity Errors

The application of least squares algorithm (which minimizes the errors in the implementation of boundary or continuity conditions at the control points) is subject to numerical error. To assess if the developed least squares solution is able to accurately implement boundary or continuity conditions throughout the computational domain, we calculate the normalized error along the evaluation surfaces at points located halfway between the control points which are initially used to construct the constrained least squares solution as follows:

$$\varepsilon_m^{\text{flux}}\ (x,y)\ = \frac{\frac{\partial\phi^-}{\partial\eta}(x,y) - \frac{\partial\phi^+}{\partial\eta}(x,y)}{\max(\text{Flux}) - \min(\text{Flux})} \qquad \text{for } m = 2, \ldots, M \qquad \text{(C.1)}$$

$$\varepsilon_m^{\text{head}}\ (x,y) = \frac{\frac{\phi^-(x,y)}{K^-} - \frac{\phi^+(x,y)}{K^+}}{H_r} \qquad \text{for } m = 2, \ldots, M \qquad \text{(C.2)}$$

where $\varepsilon_m^{\text{flux}}$ and $\varepsilon_m^{\text{head}}$ refer to normalized continuity of head and flux error across the layer interfaces.

$$\varepsilon_1^{\text{flux}}\ (x,y) = \frac{R - \frac{\partial\phi^+}{\partial\eta}(x,y)}{\max(\text{Flux}) - \min(\text{Flux})} \qquad \text{(C.3)}$$

$$\varepsilon_{M+1}^{\text{flux}}\ (x,y) = \frac{\frac{\partial\phi_M^-}{\partial\eta}(x,y)}{\max(\text{Flux}) - \min(\text{Flux})} \qquad \text{(C.4)}$$

$$\varepsilon_1^{\text{head}}\ (x,y) = \frac{H_r - \frac{\phi^+(x,y)}{K^+}}{H_r} \qquad \text{(C.5)}$$

here $\varepsilon_1^{\text{flux}}$ and $\varepsilon_{M+1}^{\text{flux}}$ are normalized flux error along the water table surface and bottom bedrock surface, respectively. $\varepsilon_1^{\text{head}}$ also refers to normalized head error along the land surface at areas in direct contact with surface water body.

$$\varepsilon^{\text{well}}\ (x,y) = \frac{\frac{\phi\ (x,y)}{K} - \frac{\phi\left(x_p, y_p\right)}{K_p}}{H_r} \qquad \text{(C.6)}$$

$\varepsilon^{\text{well}}$ is the normalized uniformity of the head errors along well screens. In the above equations, max (flux) and min (flux) [LT^{-1}] refer to the minimum and maximum flux across the top surface and H_r is the water stage of the surface water body or river. The (-) and (+) signs refer to the top and bottom of each interface, respectively. The subscript (p) refers to the reference point at the well screens where uniformity of head along the screens is assessed with respect to the head at this point.

Appendix D: Non-uniform Random Walk Particle Tracking

Similar to Delay and Bodin (2001) and Salamon *et al.* (2006) the non-uniform random walk step of a particle is then given by :

$$x_p^k = x_p^{k-1} + V_x^* \, \Delta t + \sqrt{2D_L \Delta t}\, X_L \frac{V_x^*}{|V^*|} - \sqrt{2D_T \Delta t}\, X_T \frac{V_y^*}{|V^*|} - \sqrt{2D_T \Delta t}\, X_T \frac{V_z^*}{|V^*|} \quad \text{(D.1a)}$$

$$y_p^k = y_p^{k-1} + V_y^* \, \Delta t + \sqrt{2D_L \Delta t}\, X_L \frac{V_y^*}{|V^*|} - \sqrt{2D_T \Delta t}\, X_T \frac{V_x^*}{|V^*|} - \sqrt{2D_T \Delta t}\, X_T \frac{V_z^*}{|V^*|} \quad \text{(D.1b)}$$

$$z_p^k = z_p^{k-1} + V_z^* \, \Delta t + \sqrt{2D_L \Delta t}\, X_L \frac{V_z^*}{|V^*|} - \sqrt{2D_T \Delta t}\, X_T \frac{V_x^*}{|V^*|} - \sqrt{2D_T \Delta t}\, X_T \frac{V_y^*}{|V^*|} \quad \text{(D.1c)}$$

where $|V^*| = \sqrt{{V_x^*}^2 + {V_y^*}^2 + {V_z^*}^2}$ & $D_L = \alpha_L |V^*|$ & $D_T = \alpha_T |V^*|$

D_L and D_T [L^2T^{-1}] are longitudinal and transverse hydrodynamic dispersion coefficients, and α_L and α_T [L] are longitudinal and transverse dispersivities of the porous medium, respectively. X_L and X_T are random numbers drawn from normal distributions with zero mean and unit variance for each particle and each time step (Δt). The asterisk denotes the correction of the implementation of non-uniformity in flow within the RWPT method. The corrected velocities (V_x^*, V_y^*, V_z^*) are:

$$V_x^* = V_x + \frac{\partial D_{xx}}{\partial x} + \frac{\partial D_{zx}}{\partial z} + \frac{\partial D_{yx}}{\partial y} \quad \text{(D.2a)}$$

$$V_y^* = V_y + \frac{\partial D_{yy}}{\partial y} + \frac{\partial D_{xy}}{\partial x} + \frac{\partial D_{zy}}{\partial z} \quad \text{(D.2b)}$$

$$V_z^* = V_z + \frac{\partial D_{zz}}{\partial z} + \frac{\partial D_{xz}}{\partial x} + \frac{\partial D_{yz}}{\partial y} \quad \text{(D.2c)}$$

where V_x, V_y and V_z are mean pore water velocities in *x*, *y* and *z* directions calculated using Series-AEM solution. In the above equations the tensor of dispersion is given by:

$$D_{xx} = \frac{\alpha_L V_x^2 + \alpha_T V_y^2 + \alpha_T V_z^2}{|V\,|} \tag{D.2d}$$

$$D_{yy} = \frac{\alpha_L V_y^2 + \alpha_T V_x^2 + \alpha_T V_z^2}{|V\,|} \tag{D.2e}$$

$$D_{zz} = \frac{\alpha_L V_z^2 + \alpha_T V_x^2 + \alpha_T V_y^2}{|V\,|} \tag{D.2f}$$

$$D_{xy} = D_{yx} = (\alpha_L - \alpha_T)\,\frac{V_y V_x}{|V\,|} \tag{D.2g}$$

$$D_{xz} = D_{zx} = (\alpha_L - \alpha_T)\,\frac{V_z V_x}{|V\,|} \tag{D.2h}$$

$$D_{yz} = D_{zy} = (\alpha_L - \alpha_T)\,\frac{V_z V_y}{|V\,|} \tag{D.2i}$$

where $|V\,| = \sqrt{V_x^2 + V_y^2 + V_z^2}$

The particle tracking scheme used to generate pathlines can also estimate transit time or groundwater age corresponding to each pathline and transit time distribution (TTD) of water discharged into the river and captured by the radial collector well. The simulated TTDs are the probability density function of the transit time (age) of discharging particles into the river and well. These age distributions are here fitted with a Gamma probability density function as a function of the transit time (τ):

$$p(\tau) = \frac{a(\frac{\tau}{\tau_0})^{a-1}}{\tau_0 \Gamma(a)}\, e^{-a(\frac{\tau}{\tau_0})} \tag{D.3}$$

where τ_0 is the mean groundwater age of the discharged water into the river or radial collector well, a is the Gamma shape parameter and $\Gamma(a)$ is the Gamma function. As the Gamma shape parameter decreases, the age variability of water captured in the river (or well) increases.

FIGURE 1:

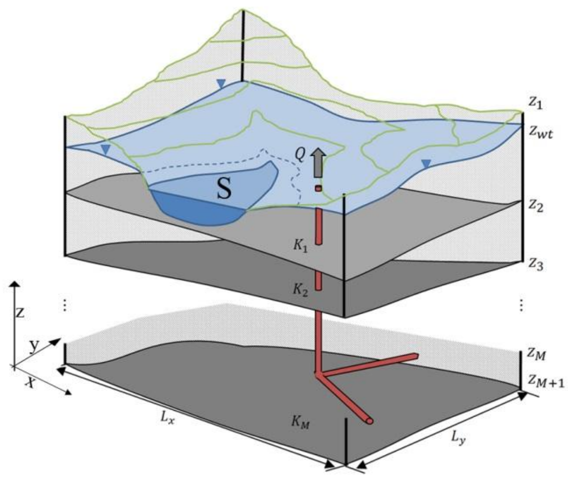

Figure 1. Layout of the general 3-D problem. The domain has a length of L_x and L_y in *x* and *y* directions, and is subdivided into M layers each with hydraulic conductivity of K_m. Layers, indexed downward from 1 to M, are bounded by the $z_m(x, y)$ above and $z_{m+1}(x, y)$ below. No-flow boundary condition is applied along the bottom bedrock $z_{M+1}(x, y)$ (at z = 0) and sides of the aquifer (x = 0 & x = L_x & y = 0 & y = L_y) . The free boundary water table surface (a priori unknown interface), $z_{wt}(x, y)$, is defined as the surface with zero pressure head calculated using an iterative scheme (Equation A.8). The predefined constant infiltration flux (*R*) is applied along the $z_{wt}(x, y)$ at each iteration. The predefined constant head boundary condition equals to the water level stage (H_r) at surface water body (S) is also applied along the predefined location of surface water bodies (e.g., lake, river). Radial horizontal arms of the same length of l_{wl} are located at the elevation of z_{wl}. The predefined pumping rate of *Q* is applied at the location of radial collector well using AEM method. The uniform head of the radial collector well (H_w) is calculated as the part of the solution.

FIGURE 2:

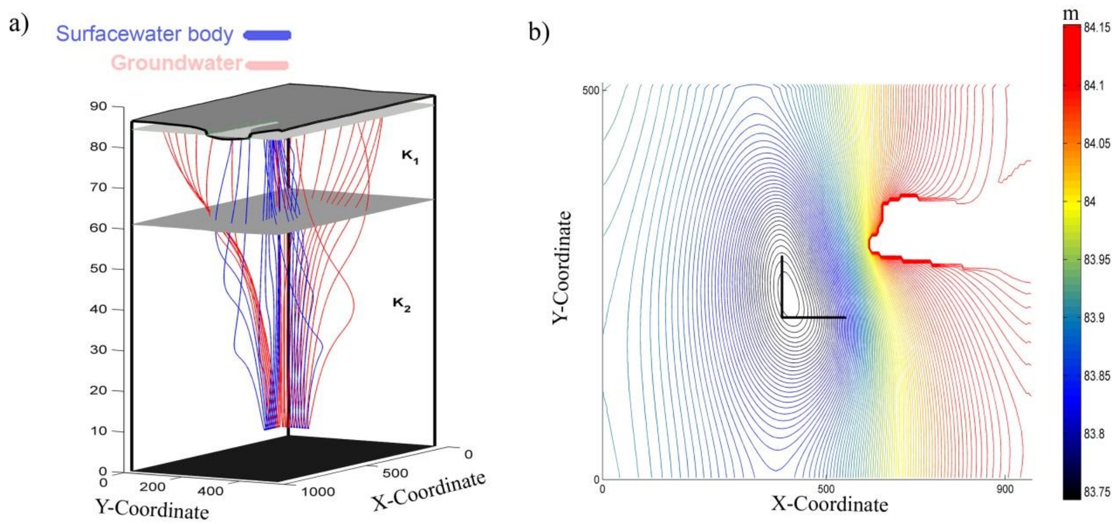

.

Figure 2. Series-AEM solution of surface water and groundwater flow toward radial collector well in a 2-Layer unconfined aquifer after 60 iterations. a) Layout of 3D flow pathlines move toward collector well originated from surface water body and groundwater. Light grey and dark grey (at the middle) surfaces depict the converged water table and the layer interface, respectively. b) Plan view of contours of converged water table surface. Angled line shows the location of the radial collector well.

FIGURE 3:

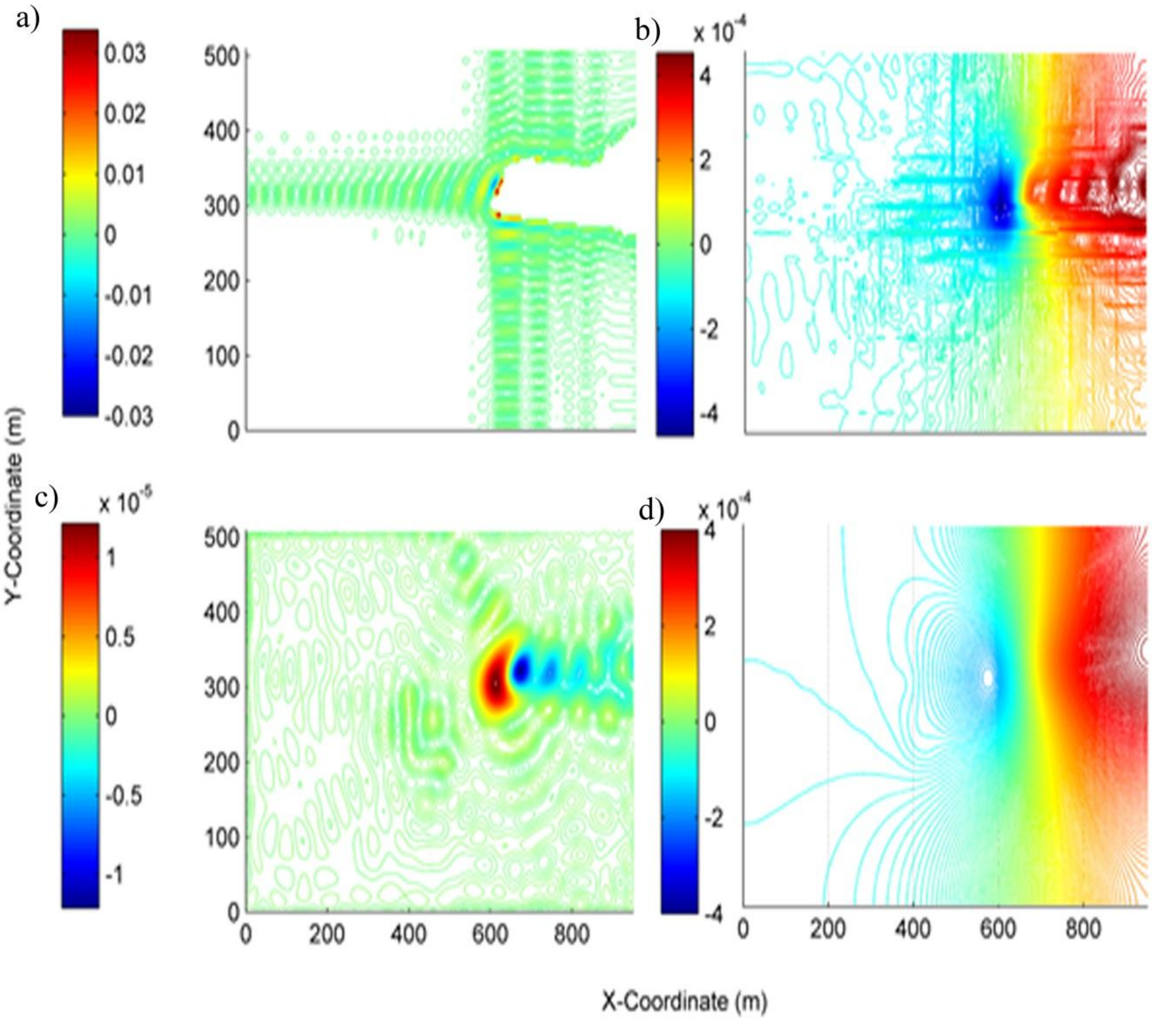

Figure 3. Normalized error in boundary and continuity conditions along the water table, bottom bedrock and layer interfaces. a) Contours of normalized flux error along the water table surface (Equation C.3) with a maximum of 3%.. b) contours of normalized continuity of flux error along the layer interface (Equation C.1) with a maximum of 0.04%. c) contours of normalized continuity of head error along the layer interface (Equation C.2) with a maximum of 10^{-3}%. d) contours of normalized flux error along the bottom bedrock (Equation C.4) (only series solution portion since the AEM portion exactly satisfies the no-flow condition across the bottom bedrock) with a maximum of 0.04%.

613 **FIGURE 4:**

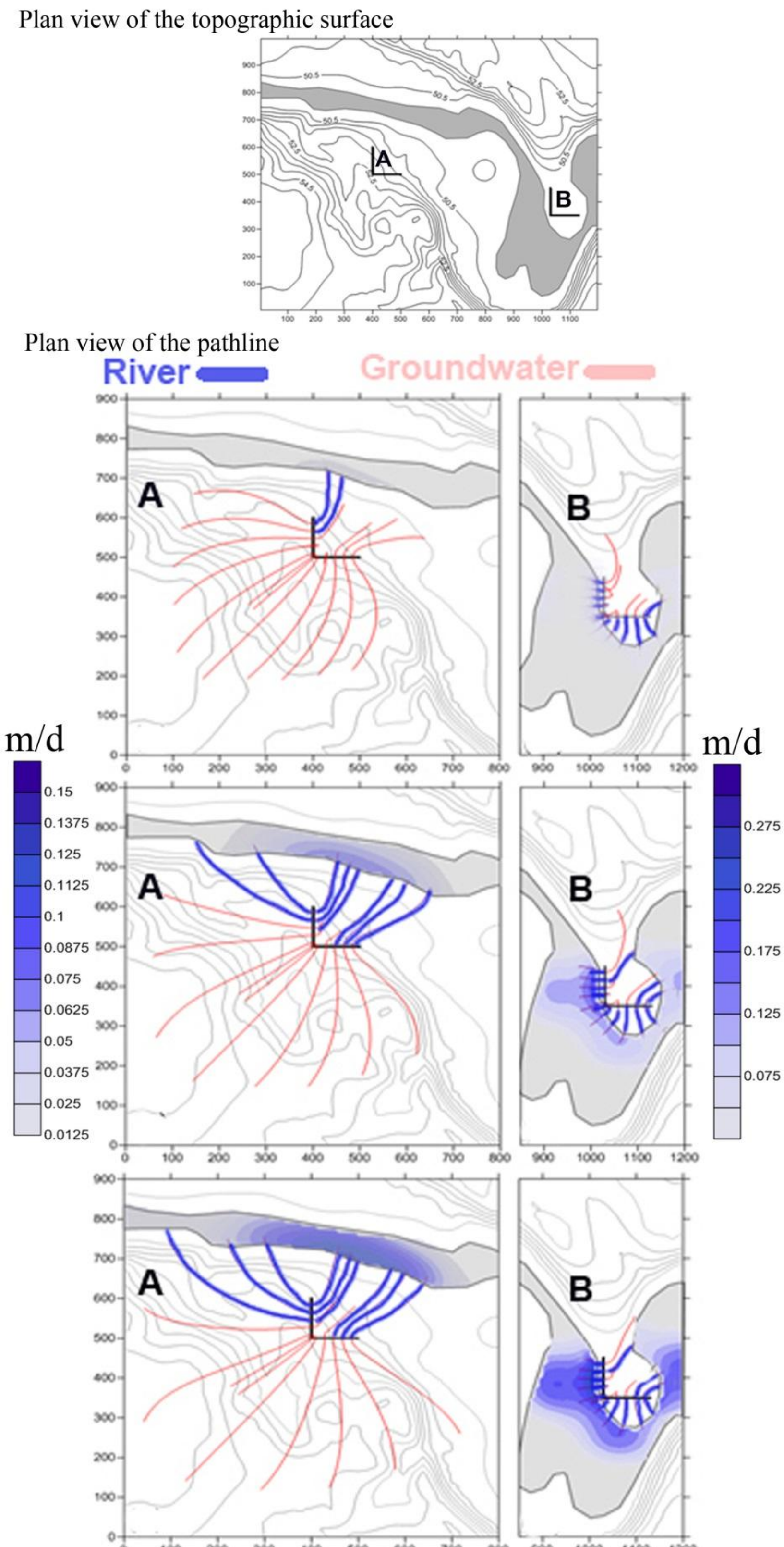

614

Figure 4. Layout of the topographic surface (top panel) and the plan view of subsurface flow pathlines in the vicinity of two radial collector well configurations (bottom panel). Right and left parts of each figure refer to the radial collector wells located in configurations A and B, respectively. Colored lines are pathlines toward radial collector wells originating from river and groundwater. The color scales depict the flux distribution (m/d) across the river bed. a&a′) Q=5000 m^3/d, b&b′) Q=10000 m^3/d and c&c′) Q=15000 m^3/d. Two different configurations, A (x=400, y=500) and B (x=1030, y=350) are considered for the caisson of the radial collector well, which consists of two arms (in x+ and y+ directions) with a length of $l_{wl} = 100\ m$, diameter of 0.50 m and an elevation of $Z_{wl} = 7\ m$. The grey lines are contours of topographic surface elevations. The vertical thickness of the domain is on average 50 m. Configuration B is located in the inner section of a bend while configuration A is further away from the bending branches of the river with an arm parallel and the other arm perpendicular to the neighboring straight branch of the river.

FIGURE 5:

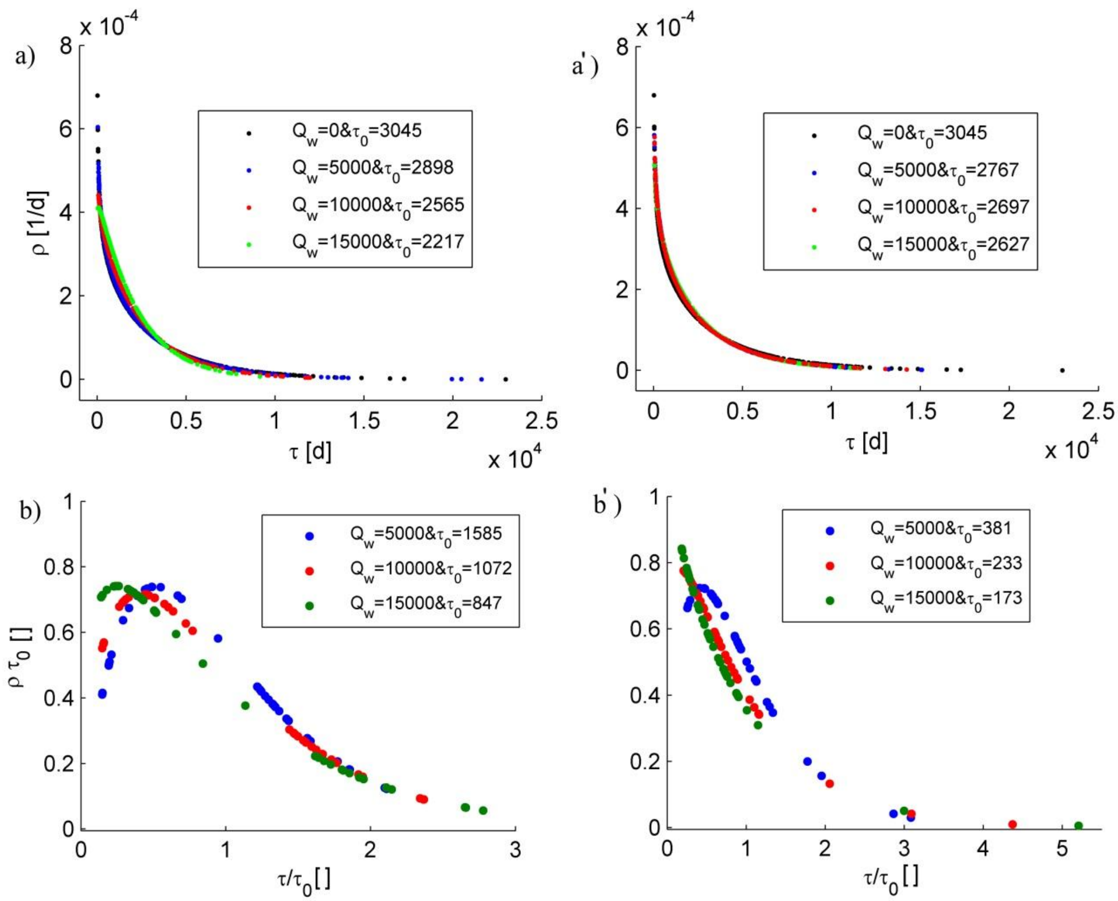

Figure 5. Effect of pumping rates Q_w [m^3/d] on the probability density function of transit times (TTD; Equation D.3) and mean age τ_0 [d] of (top panel) the groundwater discharged into the river and (bottom panel) groundwater discharged into the radial collector well. a & b). For position A of the radial collector well and a′ & b′) for position B of the radial collector well. Positions A and B of the collector well were shown in figure 4. To calculate the transit times of the water particles discharged into the river (top panel), a back tracking scheme from 440 uniformly spaced particle release points (located along the river) toward the phreatic surface was used for all cases. To calculate the transit times of the water particles discharged into the radial collector well (bottom panel), a back tracking scheme from 120 uniformly spaced particle release points located along the radial collector well screens was used for all cases. In the bottom panel, the TTDs are dimensionless TTD which were normalized with respect to mean groundwater age (τ_0), and denote the ensemble of particle transit times from both groundwater and river sources discharged into the radial collector well.

Figure A.1

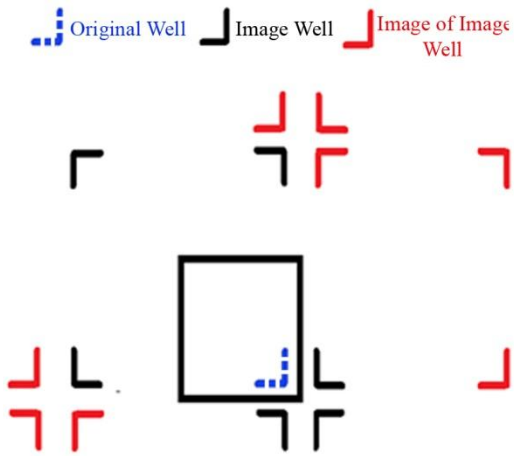

Figure A.1. Plan view of image wells method used to emulate no-flow boundary (AEM portion) of the sides of the domain. Dashed angled-shape lines represent the original radial collector well which includes two arms while continuous angled-shape lines refer to the images and the images of images radial collector well.